

Suppression of cross-track vibrations using a self-sensing micro-actuator in hard disk drives

Uwe Boettcher · Liane Matthes · Bernhard Knigge ·
Raymond A. de Callafon · Frank E. Talke

Received: 26 September 2011 / Accepted: 7 May 2012 / Published online: 1 June 2012
© Springer-Verlag 2012

Abstract In this study we utilize the self-sensing capabilities of piezoelectric micro-actuators in hard disk drives (HDD) to actively suppress in-plane resonance modes of the suspension in an HDD. The self-sensing circuit is based on a tunable capacitance bridge that decouples the control signal from the sensing signal in the micro-actuator. A hybrid modeling technique based on a realization algorithm and least-squares optimization for continuous-time systems is used to model the single-input dual-output system. An analog controller was computed using standard H_∞ -controller design tools and reduced in order using model reduction routines. Experimental implementation using analog filter design shows the effectiveness of the proposed method in reducing the main sway modes of the suspension.

Keywords Active vibration damping · Dual-stage actuator · Self-sensing-circuit

U. Boettcher (✉) · L. Matthes · R. A. de Callafon · F. E. Talke
Center for Magnetic Recording Research, University
of California, San Diego, 9500 Gilman Drive # 0401,
La Jolla, CA 92093, USA
e-mail: uwe@ucsd.edu

L. Matthes
e-mail: lmatthes@ucsd.edu

R. A. de Callafon
e-mail: callafon@ucsd.edu

F. E. Talke
e-mail: ftalke@ucsd.edu

B. Knigge
Western Digital Corporation, 5863 Rue Ferrari, San Jose,
CA 95138, USA
e-mail: bernhard.knigge@wdc.com

1 Introduction

The track density in future hard disk drives (HDD) will increase to 1 million tracks per inch in order to meet projected storage density goals. At such high density, the 3σ -value of the track mis-registration (TMR) budget is only 2–3 nm. Concurrently, the flying height in HDD as depicted in Fig. 1 is on the order of 1 nm to maintain a sufficiently high signal-to-noise ratio (SNR) during writing/reading of data. This ultra-low flying height regime is typically referred to as near contact recording. Several researchers have found that for many air bearing designs a stable flying region is followed by an unstable (bouncing) region and then followed by a (marginally) stable surfing regime as the flying height is decreased (Vakis et al. 2009; Liu et al. 2009; Zheng 2010; Yu et al. 2009; Hua et al. 2010). This close-contact region might be the desired operating range for future hard drives since flying height is at a minimum. However, intermittent contact between the recording head/thermal protrusion and the disk as shown in Fig. 1 becomes unavoidable at such close spacing. Occasional contact events excite the main resonance modes of the head/gimbal assembly and suspension. The most dominant off-track (in-plane) mode of state-of-the-art suspensions, the sway mode, has increased to 20–40 kHz through improved mechanical design and smaller dimensions. The frequency range of this off-track vibration mode is on the same order as the sampling frequency of the position error signal (PES) that is used as a position feedback for the closed-loop servo mechanism. Hence, contact induced off-track vibrations appear aliased in a conventional PES signal and are not detected accurately. If the resonance mode does occur below the Nyquist frequency of the PES, the sampling rate should be chosen at least 10 times the bandwidth of the closed-loop system (Gopal 2008). This in turn would

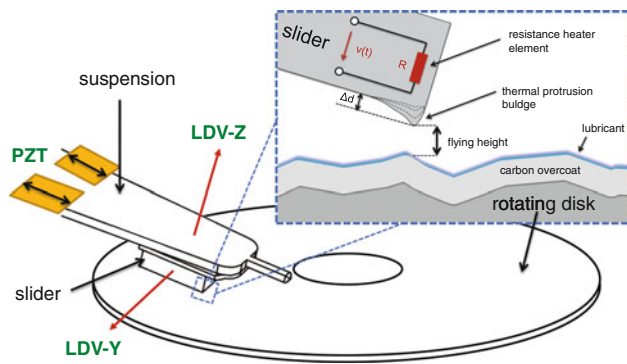


Fig. 1 Schematic of a state-of-the-art head/disk interface in a hard disk drive

require very high PES sampling rates which are not practical to be implemented. The idea of active vibration damping in hard drives has been considered for a number of years (Huang et al. 2001; Sang-Eun 1999). Multi-stage actuators that take advantage of a reduced “moving mass” compared to a single actuator design seem to be a promising approach in increasing the frequency response. Modern high storage density HDD use dual-stage actuators consisting of a conventional voice coil motor for coarse positioning and a micro actuator for fine positioning (Fig. 2c) to increase the closed-loop servo performance (Huang et al. 2005). The micro actuators used typically consist of two piezoelectric transducers (PZT) that are attached to base of the suspension as indicated in Figs. 1 and 2. One of the PZT elements contracts and one expands as a voltage is applied to the actuator. This results in a rotary motion of the recording slider with respect to the data track center. The

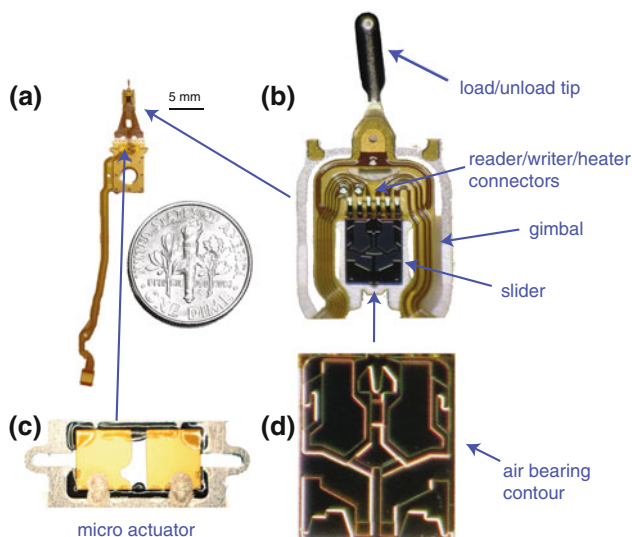


Fig. 2 a Head-gimbal assembly in a dual-stage actuator hard disk drive and magnified views of b the tip of the head-gimbal assembly, c micro actuator and d air bearing surface

head-gimbal assembly that we use in this study is depicted in Fig. 2.

In addition to actuation, PZT materials can also be used to sense strain. Using a self-sensing circuit, one can decouple actuation from sensing and, therefore, actively dampen in-plane suspension modes. The purpose of this paper is to show how an automated continuous-time modeling procedure and a subsequent controller design procedure can utilize the sensing capabilities of the PZT in an HDD to significantly improve the frequency response of the actuator. Since the computed controller is analog, there is no practical implementation limit on the closed-loop bandwidth up to the several 100 kHz regime.

2 Self-sensing piezo-electric actuator

2.1 Motivation

Extensive research has been performed on the utilization of PZT actuators to dampen vibrations (Huang et al. 2005; Roberto et al. 2007; Yunfeng et al. 2006; Yuan et al. 2010). Those active vibration damping approaches typically require additional strain sensors. This, in turn, introduces an additional degree of freedom since it is possible to place the sensor at a different location than the actuator. However, the latter approach adds to the overall cost which might in turn outweigh the actual benefits obtained in improving the frequency response. In addition to active vibration damping, passive damping approaches have also been studied. In passive damping additional viscoelastic damping layers are positioned underneath the piezo-electric elements (Chan et al. 2008). Another very interesting passive damping approach is described in (Moheiman 2003) where energy dissipation of mechanical vibrations is accomplished through shunting the piezoelectric transducer to an electrical impedance. Hence, an impedance is designed rather than a closed-loop controller (Moheiman 2003). As shown in Lee et al. (2006), it is possible to greatly dampen the resonance modes of the actuator arm by using the PZT elements as sensors only and the VCM as the sole actuator employing multi-rate control techniques.

In this paper, we will focus on a so-called “self-sensing-actuation” approach (Pang et al. 2004, 2010), in which the PZT is used as a sensor and as an actuator (Lee et al. 2006).

2.2 Self-sensing circuit

The main task of the self-sensing approach is the decoupling of sensing and actuation signal of the PZT. Many different approaches have been presented in the past and will be briefly reviewed in this subsection. A number of approaches are based on the idea that the impedance of the

PZT changes as external forces are applied. In Kawamata et al. (2008), the permittivity change is detected by injecting an input signal that was perturbed with a small amplitude, high frequency sinusoidal signal. The output current is then measured using a current probe and a lock-in amplifier allows the extraction of the sensing frequency at a high signal-to-noise ratio. This approach has been used for low frequency positioning stages that do not exceed the several 100 Hz regime. Another approach is using bridge circuits which can greatly improve the sensitivity of the measurement. Two possible circuits are shown in Fig. 3 where either velocity (strain rate) or displacement (strain) are detected (Dosch et al. 1992). This approach is based on the idea that the piezo-electric material could be approximated by a voltage source V_p in series with a capacitance C_p as indicated by the dashed lines in Fig. 3. The generated voltage V_p depends on the external forces applied to the piezo. The circuit needs to be balanced at all times. This is accomplished in the strain rate circuit (Fig. 3a) by matching the time constants ($R_1C_1 = R_2C_p$). It is slightly more difficult to balance the strain sensing circuit (Fig. 3b) since a capacitance match is required ($C_1 = C_p$). In this study, we use the strain self-sensing circuit after adding resistors to avoid DC-shift problems (Jones et al. 1994). Furthermore, the PZT needs to be referenced to electrical ground which is the case for the commercially available HGA (Fig. 2) we used in this study. The modified bridge circuit is shown in Fig. 4. The capacitance C^*_p in Fig. 4 must match the capacitance of the PZT for accurate self-sensing. This introduces an additional challenge since the capacitance of the PZT varies as a function of parameters such as pre-load, electrical charge and temperature.

2.3 Temperature dependence of PZT capacitance

The dependence of the capacitance on the temperature of the PZT used in this study is depicted in Fig. 5. The head-gimbal-assembly (HGA) was placed in a laboratory oven and exposed to a known temperature profile while measuring the capacitance. One can clearly see from Fig. 5 that in the typical temperature range of an HDD (120 °C), the capacitance increases in a linear fashion at a rate of ≈ 4 pF/°C. In our experiments we manually tuned the

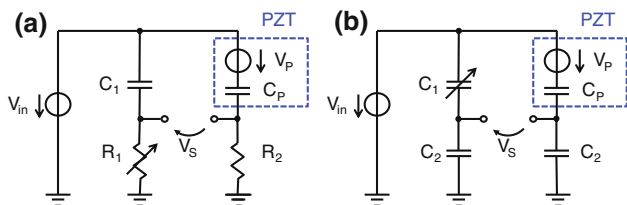


Fig. 3 Self-sensing circuits for a strain rate (“velocity”) and b strain (“displacement”) sensing

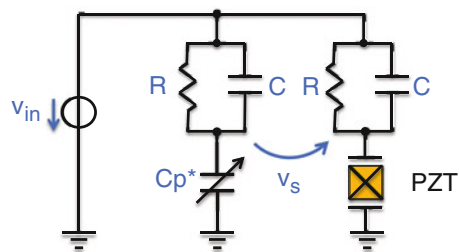


Fig. 4 Bridge circuit for strain sensing

circuit. However, automated balancing methods are available that have been developed (Kuiper 2010).

2.4 Hysteresis effects

It should be noted that most piezo-electric materials exhibit a hysteresis between generated charge due to external forces and the actual generated voltage (Adriaens et al. 2000). This is partially attributed to permittivity change in the material. Charge amplifier based sensing approaches such as discussed in (Lee and Sohn 2006) greatly reduce this hysteresis effect. However, this requires electrical access to both PZT terminals. This would require an additional connector pad compared to a single-ended (referenced to ground) PZT. The latter approach is less expensive and therefore more likely to be implemented in a hard disk drive.

3 Dynamic modeling based on frequency response measurements

In order to proceed with the design of an optimal controller, an accurate model of the plant is needed. Furthermore, a fast and automated modeling procedure is desirable to be able to accommodate to parameter variations between different head-gimbal-assemblies used in this study. The

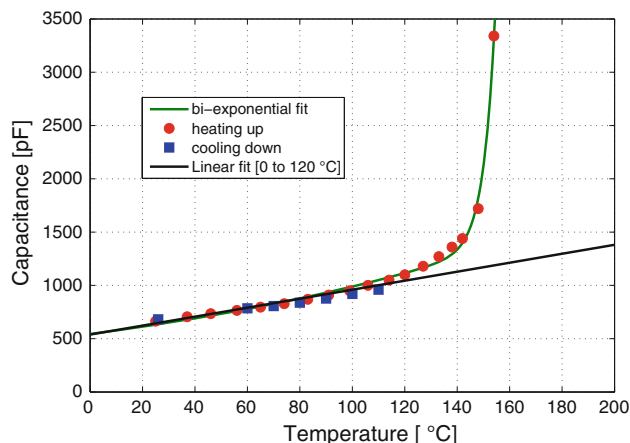


Fig. 5 Temperature dependency of PZT capacitance

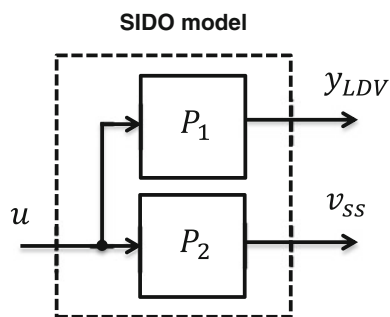


Fig. 6 Single-input dual-output dynamic model of the micro-actuator and self-sensing circuit

schematic of the model to be estimated is shown in Fig. 6. Here, P_1 represents the dynamics from the input voltage u of the actuator to the (off-track) head position y_{LDV} . P_2 represents the dynamics from input u to the output voltage of the self-sensing circuit v_{SS} . It is important to note that P_1 and P_2 have major dynamics in common since they are part of the same mechanical structure. Hence, our aim is to estimate a model of a single-input dual-output (SIDO) system of the micro-actuator and self-sensing circuit combined. A schematic of the experimental set-up and the dynamic modeling procedure is depicted in Fig. 7. The head-gimbal-assembly is loaded onto the top surface of a magnetic disk that is spinning at 7,200 rpm. As indicated in Fig. 7, a dynamic signal analyzer is used to measure the frequency response functions $\hat{P}_1(j\omega)$ and $\hat{P}_2(j\omega)$, respectively, where $\omega = [0, \dots, 50,000] \cdot 2\pi \text{rad/s}$. The actual dynamic modeling procedure is based on a combination of a subspace method and a prediction error based method as used in (Claes et al. 2007; Boettcher et al. 2010). The method will be summarized here and the interested reader is referred to (Claes et al. 2007) for further details. The steps for the system identification procedure are as follows:

1. Take inverse discrete time Fourier transform of the frequency response measurements to obtain the impulse response coefficients (Markov parameters) of the system which are defined by

$$p_{i,k} = \frac{1}{2N} \sum_{l=0}^{2N-1} \hat{P}_{i,l} e^{j\omega_k l}, \quad k = 0, 1, \dots, 2N-1 \quad (1)$$

where \hat{P}_i contains the measured frequency response data for the slider off-track position ($i = 1$) and self-sensing output ($i = 2$). In (1), ω_k is the frequency vector defined by

$$\omega_k = \frac{\pi k}{N}, \quad k = 0, 1, \dots, 2N-1 \quad (2)$$

where N denotes the number of frequency points in the frequency response measurement.

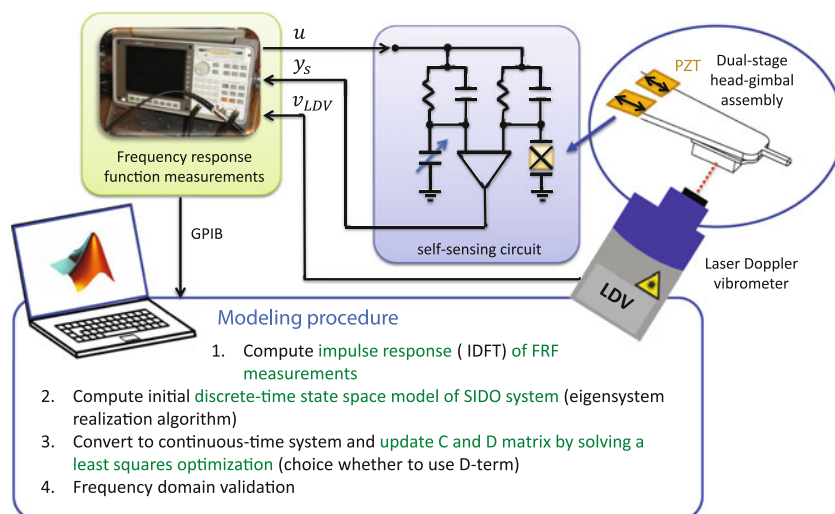
2. Store the computed impulse response coefficients in a $2m \times m$ Hankel matrix $\{\mathbf{H}\}$ defined by

$$\mathbf{H} = \begin{bmatrix} p_1(1) & p_1(2) & \cdots & p_1(m) \\ p_2(1) & p_2(2) & \cdots & p_2(m) \\ p_1(2) & p_1(3) & \cdots & p_1(m+1) \\ p_2(2) & p_2(3) & \cdots & p_2(m+1) \\ \vdots & \vdots & \vdots & \vdots \\ p_1(m) & p_1(m+1) & \cdots & p_1(2m-1) \\ p_2(m) & p_2(m+1) & \cdots & p_2(2m-1) \end{bmatrix} \quad (3)$$

where m is the number of impulse response samples taken into account. As shown in (Claes et al. 2007), one can estimate system matrix \mathbf{A}_d and input matrix \mathbf{B}_d of a discrete-time state space system utilizing the shift property in Hankel matrix structures.

3. Convert estimated discrete-time model to continuous-time assuming zero-order-hold by inverting the relations $\mathbf{A}_d = e^{\mathbf{A}\Delta T}$ and $\mathbf{B}_d = \int_0^{\Delta T} e^{\mathbf{A}\eta} d\eta \mathbf{B}$, respectively, using the matrix logarithm (Hara 2010). Here, ΔT

Fig. 7 Schematic of dynamic modeling procedure



represents the sampling time of the discrete-time system.

- Update zeros, i.e. \mathbf{C} and (if needed) \mathbf{D} matrix using standard least squares optimization. The plant model can be computed as

$$P_i(j\omega) = \mathbf{C}_i(j\omega\mathbf{I} - \mathbf{A})^{-1}\mathbf{B} + \mathbf{D}_i \tag{4}$$

where \mathbf{C}_i and \mathbf{D}_i represents the i th row of \mathbf{C} and \mathbf{D} , respectively. This can be written as a linear regression

$$P_i(j\omega) = \underbrace{[\mathbf{C}_i \quad \mathbf{D}_i]}_{\Theta_i} \underbrace{\begin{bmatrix} (j\omega\mathbf{I} - \mathbf{A})^{-1}\mathbf{B} \\ \mathbf{I} \end{bmatrix}}_{\varphi(\omega)} \tag{5}$$

with parameter vector Θ_i and regressor $\varphi(\omega)$. To avoid dealing with complex numbers in the least squares estimate we consider the real and imaginary part and define a modified version of $\varphi(\omega)$

$$\tilde{\varphi}(\omega) = \begin{bmatrix} \Re\{(j\omega\mathbf{I} - \mathbf{A})^{-1}\mathbf{B}\} & \Im\{(j\omega\mathbf{I} - \mathbf{A})^{-1}\mathbf{B}\} \\ \mathbf{I} & 0 \end{bmatrix} \tag{6}$$

and in the same fashion for the frequency response measurements P_i

$$\tilde{P}_i = [\Re\{P_i\} \quad \Im\{P_i\}] \tag{7}$$

We can now define the error by

$$\epsilon_i(\Theta_i, \omega) = \Theta_i \tilde{\varphi} - \tilde{P}_i \tag{8}$$

and finally compute Θ_i by solving a least-squares optimization

$$\Theta_i = \tilde{P}_i \tilde{\varphi}^T (\tilde{\varphi} \tilde{\varphi}^T)^{-1} \tag{9}$$

In case there is no feedthrough term \mathbf{D} estimated, the last row in (6) is deleted.

- Perform frequency domain validation based on frequency response function measurements and the estimated model

This procedure results, unlike in Boettcher et al. (2010) or Claes et al. (2007), in a continuous-time model of the single-input dual-output system. One of the model parameters is the order n . In order to model all the system dynamics sufficiently well, a relatively high model order is desired. Figure 8 (top) shows the singular values of the Hankel matrix \mathbf{H} in (3) and the squared estimation errors in (8) as a function of the estimated model order. This measure helps in choosing the appropriate model order n . As expected, the estimation error decreases as the model order is increased. However, there is a clearly visible demarcation where a further increase in model order does not decrease the estimation error further. Therefore, we chose a relatively high 20th order model knowing that

order reduction routines will later be applied to the computed controller. Figure 9 shows the Bode plot of the frequency response measured and estimated for P_1 (top) and P_2 (bottom), respectively. From Fig. 9 we observe excellent agreement between measurement and simulated frequency response. The largest peak in both bode plots in Fig. 9 corresponds to the sway mode at 19.7 kHz and the second largest peak at around 15 kHz is presumably related to the flex cable.

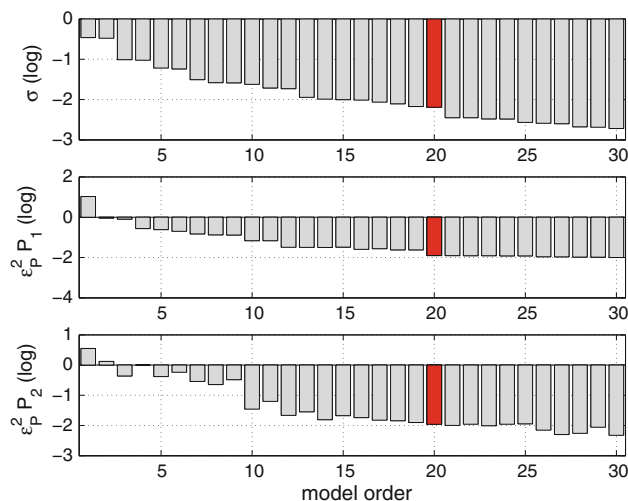


Fig. 8 Plot of singular values (top row) and least squares error of estimating the zeros of P_1 (middle row) and P_2 (bottom row) as a function of the estimated model order

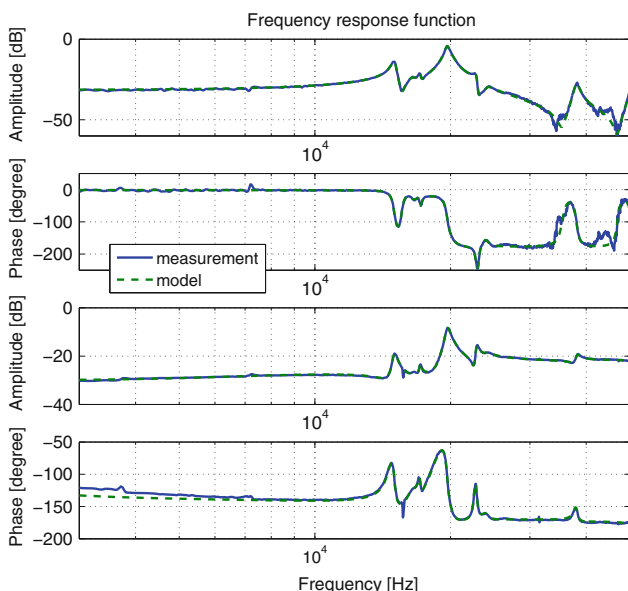


Fig. 9 Measured frequency response function and estimated continuous-time model of P_1 (top) and P_2 (bottom)

4 Controller design and order reduction

The aim is to compute an H_∞ optimal controller K that minimizes output vibrations on y_{LDV} as indicated in Fig. 10. In addition, we take the control energy into account and compute the controller K by solving

$$K = \arg \min_{\tilde{K}} \left\| \begin{bmatrix} \frac{P_1}{1+KP_2} \\ \frac{\alpha \tilde{K}}{1+KP_2} \end{bmatrix} \right\|_\infty \quad (10)$$

where α is the control weighting. The larger the value we choose for α , the smaller the damping improvement we obtain. We can solve (10) using Matlab’s Robust Control Toolbox which solves the problem based on the two-Riccati formulae (Glover 1988; Doyle et al. 1989) and loop-shifting (Safonov et al. 1989). This can be done by re-defining the plant model as indicated in Fig. 11 to include the weighted control signal output. The re-defined state space mode simply yields

$$\dot{x}(t) = \mathbf{A}x(t) + \begin{bmatrix} \mathbf{B} & -\mathbf{B} \end{bmatrix} \begin{bmatrix} r \\ u \end{bmatrix} \quad (11)$$

$$y = \begin{bmatrix} 0 \\ \mathbf{C} \end{bmatrix} + \begin{bmatrix} 0 & \alpha \\ \mathbf{D} & -\mathbf{D} \end{bmatrix} \begin{bmatrix} r \\ u \end{bmatrix}$$

where $\mathbf{A}, \mathbf{B}, \mathbf{C} = [\mathbf{C}_1^T \ \mathbf{C}_2^T]^T$ and $\mathbf{D} = [\mathbf{D}_1 \ \mathbf{D}_2]^T$ represents the state space matrices of the originally estimated continuous-time model in Sect. 3 and the new output is defined as $y = [u_w \ y_{LDV} \ v_{SS}]$. The computed controller K is of the same order as the estimated SIDO model, in our case 20th order. This is impractical for implementation. Hence, the order of the controller is reduced using implicitly balanced model order reduction (Varg 1991). This ensures also that the reduced order model remains stable. The results of the controller order reduction are shown in Fig. 12. Figure 12 shows that the main dynamics

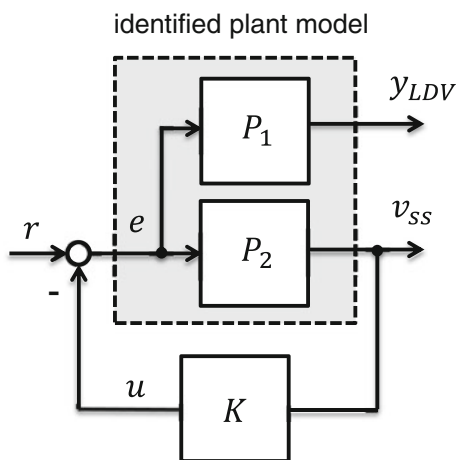


Fig. 10 Closed-loop system

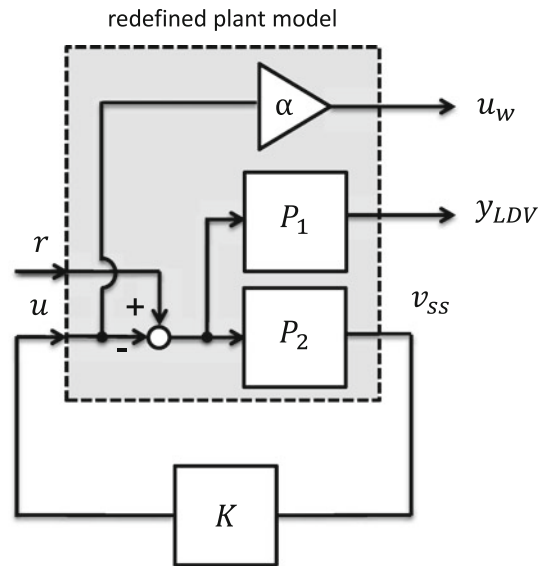


Fig. 11 Closed-loop system with redefined plant

of the high order controller are described very well using a 4th order approximation. Hence, the closed-loop transfer dynamics are about the same for both controllers as seen in Fig. 13. The choice of the control effort weighting α is crucial to the performance of the controller. Figure 14 shows the computed closed-loop transfer function for $\alpha = 0.22$, $\alpha = 0.18$ and $\alpha = 0.14$ compared to the original

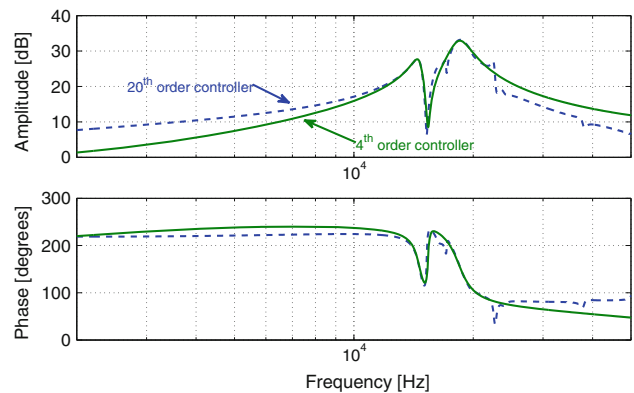


Fig. 12 20th order controller and reduced 4th order controller

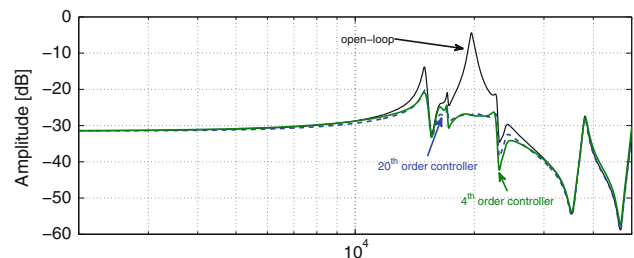


Fig. 13 Modeled open-loop transfer function (P_1) and closed-loop transfer function computed for 4th and 20th order controller

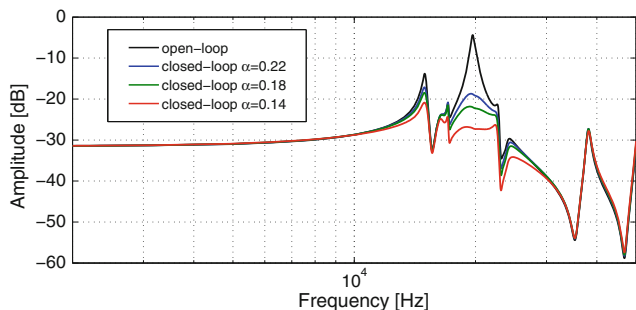


Fig. 14 Damping improvement of the closed-loop system as a function of the control weighting α in (10)

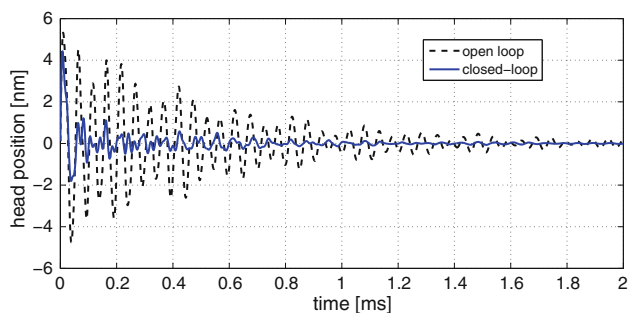


Fig. 15 Computed impulse response of open-loop model P_1 and closed-loop system for $\alpha = 0.14$

open-loop response of P_1 (black solid line). One can see that the smallest value for α leads the best damping results. However, this comes at the expense of larger control signals. The computed impulse response for the open-loop and the closed-loop system for $\alpha = 0.14$ is shown in Fig. 15. We can observe a great improvement in terms of damping and settling time as expected.

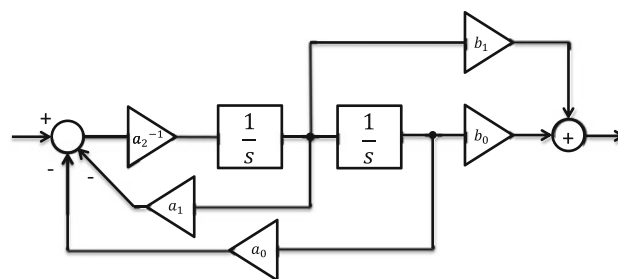


Fig. 16 Canonical form of second order filter

5 Practical controller realization and implementation results

A digital controller at high sampling rates would likely be too expensive to be feasible in a large quantity low-cost data storage device such as a hard disk drive. Instead, we design an analog circuit with the transfer characteristics of the computed 4th order controller as shown in Fig. 12. First, the fourth order filter is separated into two second order filters plus a constant term k using partial fractional expansion:

$$K = k + \sum_{i=1}^2 \frac{b_{1,i}s + b_{0,i}}{a_{2,i}s^2 + a_{1,i}s + a_{0,i}} \quad (12)$$

There are many different ways to design a circuit that realizes (12). We base our design on the standard canonical form as shown in Fig. 16. This is not efficient in terms of number of parts used, but very convenient to tune as only five potentiometers are needed to adjust the five parameters in (12). It should be noted that the additional degree of freedom in a_2 is only needed for signal conditioning reasons within the circuit. We have realized this circuit using

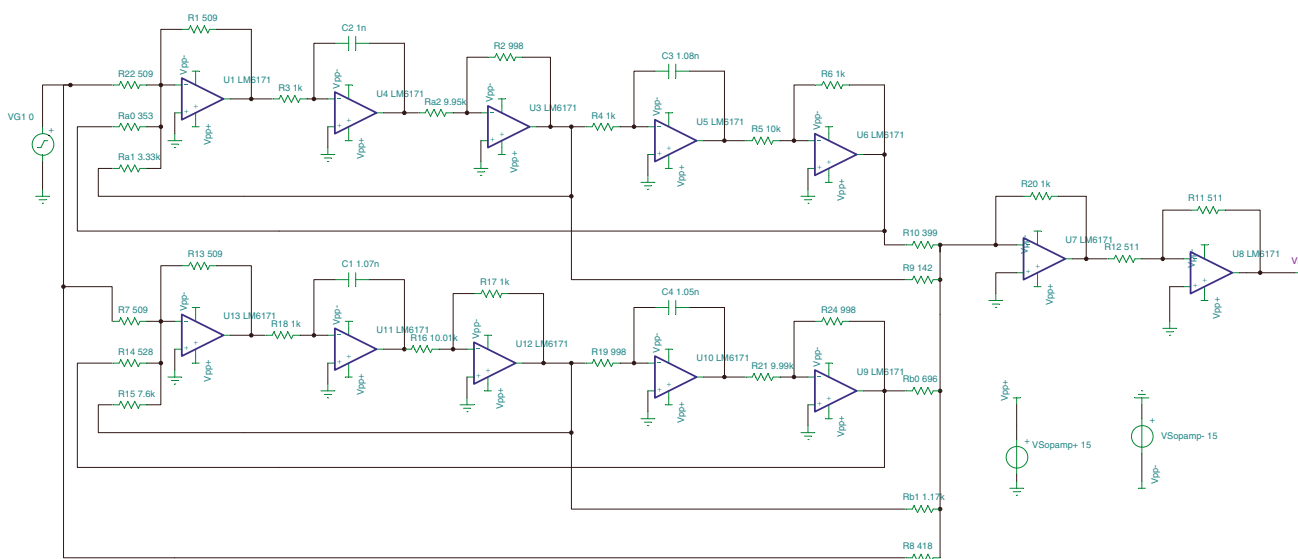


Fig. 17 SPICE schematic of the prototype circuit

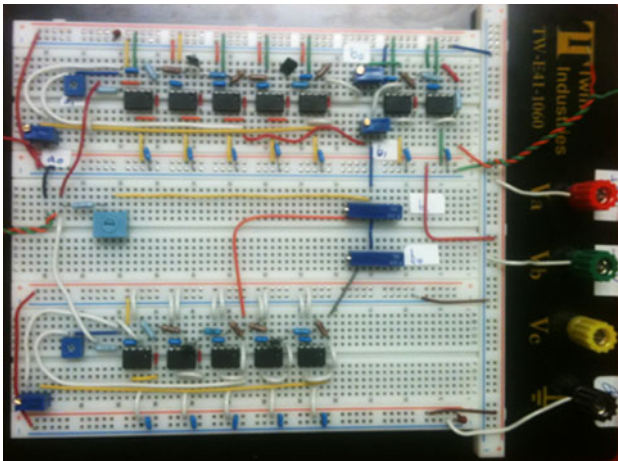


Fig. 18 Implemented prototype of 4th order controller on a “breadboard”

12 high slew rate (but voltage feedback) operational amplifiers of type LM6171. The spice schematic is shown in Fig. 17 and the actual controller prototype on the bread board is shown in Fig. 18. Figure 19 shows a comparison of the theoretical filter response, the spice model (simulated) and the measured response of the actual prototype. From Fig. 19 we observe that the theoretical response and the SPICE model response are in excellent agreement.

The controller shown in Fig. 19 was implemented in the experimental set-up and the frequency response function was measured to compare it to the initial open-loop response. The measured frequency response for open-loop and closed-loop system are compared in Fig. 20. One can see from Fig. 20 that the improvement of the frequency response is significant in terms of active damping of two major off-track modes of the suspension.

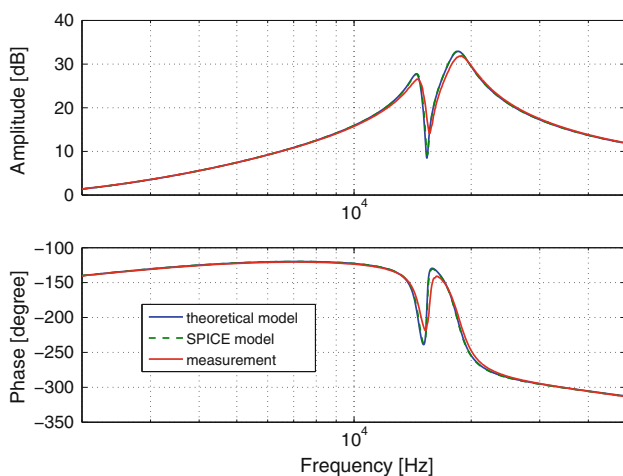


Fig. 19 Bode response of analog controller

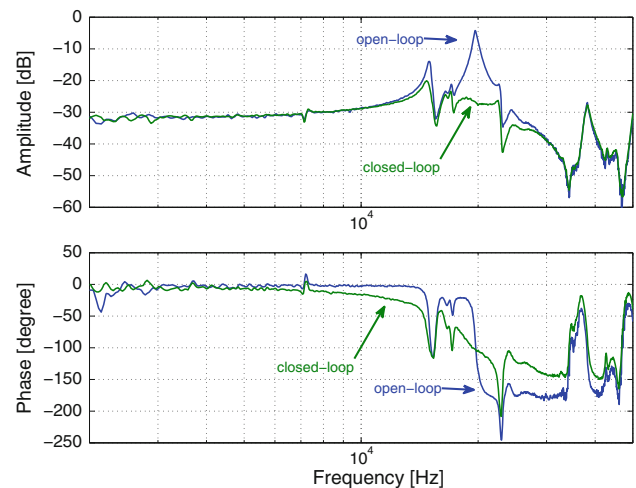


Fig. 20 Measured frequency response of open-loop and closed-loop system for controller implemented for $\alpha = 0.14$

6 Conclusions

Strain self-sensing bridge circuits were found to be useful to measure in-plane head-gimbal-assembly modes. However, the circuit was seen to be sensitive to parameter variations in the PZT. The PZT capacitance is a strong function of temperature but increases in a linear fashion within the operating range of an HDD. Therefore, an adjustable approach is needed that keeps the self-sensing circuit balanced at all times. Charge amplifier based approaches featuring reduced hysteresis effects might yield improved sensing results but require electrical non-referenced access to the PZT. An hybrid automated modeling procedure was developed based on a realization algorithm and least squared error based optimization. The estimated continuous-time models are in excellent agreement with the measured frequency response. A 4th order analog controller was designed using standard H_∞ design methods and an order reduction routine. The controller was implemented in the experimental set-up and showed excellent improvement in terms of damping the main off-track modes of the HGA. This might significantly reduce off-track vibrations that result from contact between the head and the disk (e.g. during load/unload) or to compensate for windage disturbances. Collocated micro-actuator designs that feature the PZT closer to the slider might increase the frequency response of the vibration detection to allow active vibration damping up to the multiple 10 kHz regime.

Acknowledgments We would like to thank John Hogan of NHK International Corp. for his interest in this work and for help with identifying the resonance modes of the suspension.

References

- Adriaens HJMTS, De Koning WL, Banning R (2000) Modeling piezoelectric actuators. *IEEE/ASME Trans Mechatron* 5(4): 331–341. doi:10.1109/3516.891044
- Baek S-E, Lee S-H (1999) Vibration rejection control for disk drives by acceleration feedforward control. In: Proceedings of the 38th IEEE conference on decision and control, vol 5, pp 5259–5262
- Boettcher U, De Callafon RA, Talke FE (2010) Modeling and control of a dual stage actuator hard disk drive. *J Adv Mech Design Syst Manuf* 4(1):107–118
- Chan KW, Liao WH, Shen IY (2008) Precision positioning of hard disk drives using piezoelectric actuators with passive damping. *IEEE/ASME Trans Mechatron* 13(1):147–151
- Claes M, Graham MR, de Callafon RA (2007) Frequency domain subspace identification of a tape servo system. *Microsyst Technol* 13:1439–1447
- Gopal (2008) Digital control and state variable method. 2nd edn. McGraw-Hill pvt ltd., India. ISBN: 9780070668805. <http://books.google.com/books?id=Y1d02O6q4qoC>
- Dosch JJ, Inman DJ, Garcia E (1992) A self-sensing piezoelectric actuator for collocated control. *J Intell Mater Syst Struct* 3:166–185
- Doyle JC, Glover K, Khargonekar P, Francis B (1989) State-space solutions to standard H2 and H control problems. *IEEE Trans Autom Control* 34(8):831–847
- Glover K, Doyle JC (1988) State-space formulae for all stabilizing controllers that satisfy an Hnorm bound and relations to risk sensitivity. *Syst Control Lett* 11:167–172
- Hara S (2010) Perspectives in mathematical system theory, control, and signal processing: a festschrift in honor of Yutaka Yamamoto on the occasion of his 60th birthday. In: Lecture notes in control and information sciences. Springer, Berlin, vol 398
- Horowitz R, Li Y, Oldham K, Kon S, Huang X (2007) Dual-stage servo systems and vibration compensation in computer hard disk drives. *Control Eng Practice* 15(3):291–305 (Selected Papers Presented at the Third IFAC Symposium on Mechatronic Systems (2004), Third IFAC Symposium on Mechatronic Systems)
- Hua W, Liu B, Yu S, Zhou W (2010) Contact recording review. *Microsyst Technol* 16:493–503
- Huang F-Y, Semba T, Imano W, Lee F (2001) Active damping in HDD actuator. *IEEE Trans Magn* 37(2):847–849
- Huang X, Horowitz R, Li Y (2005) Track-following control with active vibration damping and compensation of a dual-stage servo system. *Microsyst Technol* 11(12):1276–1286
- Jones L, Garcia E, Waites H (1994) Self-sensing control as applied to a PZT stack actuator used as a micropositioner. *Smart Mater Struct* 3(2):147–156
- Kawamata A, Kadota Y, Hosaka H, Morita T (2008) Self-sensing piezoelectric actuator using permittivity detection. *Ferroelectrics* 368:194–201
- Kuiper S, Schitter G (2010) Active damping of a piezoelectric tube scanner using self-sensing piezo actuation. *Mechatronics* 20(6):656–665 (ISSN 0957–4158)
- Lee SJ, Sohn H (2006) Active self-sensing scheme development for structural health monitoring. *Smart Mater Struct* 15:1734
- Lee S-H, Chung CC, Lee CW (2006) Active high-frequency vibration rejection in hard disk drives. *IEEE/ASME Trans Mechatron* 11(3):339–345
- Li Y, Marcassa F, Horowitz R, Oboe R, Evans R (2006) Track-following control with active vibration damping of a PZT-actuated suspension dual-stage servo system. *J Dyn Sys Meas Control* 128:568
- Liu B, Zhang MS, Yu SK, Hua W, Ma YS, Zhou WD, Gonzaga L, Man YJ (2009) Lube-surfing recording and its feasibility exploration. *IEEE Trans Magn* 45(2):899–904
- Moheimani SOR (2003) A survey of recent innovations in vibration damping and control using shunted piezoelectric transducers. *IEEE Trans Control Syst Technol* 11(4):482–494
- Pang CK, Guo G, Chen BM, Lee TH (2004) Nanoposition sensing and control in HDD dual-stage servo systems. *IEEE Int Conf Control Appl* 1:551–556
- Pang CK, Hong F, Wong WE, Lee TH (2010) Self-sensing actuation for piezoelectric and mems devices in data storage applications. In: DST-CON
- Safonov MG, Limebeer DJN, Chiang RY (1989) Simplifying the H theory via loop shifting, matrix pencil and descriptor concepts. *Int J Contr* 50(6):2467–2488
- Vakis AI, Sung-Chang Lee, Polycarpou AA (2009) Dynamic head-disk interface instabilities with friction for light contact (surfing) recording. *IEEE Trans Magn* 45(11):4966–4971
- Varga A (1991) Balancing-free square-root algorithm for computing singular perturbed approximations. In: Proceedings of 30th IEEE CDC Brighton, UK, pp 1062–1066
- Yu SK, Liu B, Zhou WD, Hua W, Gonzaga L (2009) Dynamic stability analysis for surfing head-disk interface. *IEEE Trans Magn* 45(11):4979–4983
- Yuan Y, Du H, Wang S (2010) A miniature in-plane piezoresistive mems accelerometer for detection of slider off-track motion in hard disk drives. *Microsyst Technol* 16:931–940
- Zheng J, Bogy D (2010) Investigation of flying-height stability of thermal fly-height control sliders in lubricant or solid contact with roughness. *Tribol Lett* 38:283–289